

Milan Banjac¹

Faculty of Mechanical Engineering,
University of Belgrade,
Belgrade 11120, Serbia
e-mail: mbbanjac@mas.bg.ac.rs

Teodora Savanovic

Faculty of Mechanical Engineering,
University of Belgrade,
Belgrade 11120, Serbia
e-mail: tsavanovic@mas.bg.ac.rs

Djordje Petkovic

Faculty of Mechanical Engineering,
University of Belgrade,
Belgrade 11120, Serbia
e-mail: dpetkovic@mas.bg.ac.rs

Milan V. Petrovic

Faculty of Mechanical Engineering,
University of Belgrade,
Belgrade 11120, Serbia
e-mail: mpetrovic@mas.bg.ac.rs

A Comprehensive Analytical Shock Loss Model for Axial Compressor Cascades

The approach applied in various research papers that model compressor shock losses is valid only for certain types of airfoil cascades operating in a narrow range of working conditions. Lately, more general shock loss models have been established that cover a wider variety of airfoils and operating regimes. However, owing to the complexity of the studied matter, the majority of such models are, to a certain extent, presented only in a descriptive manner. The lack of specific details can affect the end results when such a model is utilized since improvisation cannot be avoided. Some models also apply complex numerical procedures that can slow the calculations and be a source of computational instability. In this research, an attempt has been made to produce an analytical shock loss model that is simple enough to be described in detail while being universal and robust enough to find wide application in the fields of design and performance analysis of transonic compressors and fans. The flexible description of airfoil geometry encompasses a variety of blade shapes. Both unchoked and choked operating regimes are covered, including a precise prediction of choke occurrence. The model was validated using a number of numerical test cases. [DOI: 10.1115/1.4053852]

Keywords: fan, compressor, shock loss, choke angle, blade design

Introduction

Shock wave-produced total pressure drop is one of the main loss generation mechanisms in high-speed axial fans and compressors. Furthermore, it can significantly influence the process in industrial low-speed machines if the critical Mach number has been reached locally. Although such phenomena can be captured by applying planar cascade flow solvers and three-dimensional computational fluid dynamics, the literature still lacks classic models for shock losses, which can manage a broader set of blade geometry parameters and operating conditions. This is necessary for performing precise throughflow calculations that are used for compressor and fan design, performance analysis, and transient simulations of overall gas turbine engines.

Seminal research in the area of shock loss modeling considers limited types of cascades and operating regimes. Miller et al. [1] described loss generation for a double circular arc (DCA) cascade operating with supersonic inlet and inflow angles close to the design values. The given description of the detached dual shock wave system formed in an unchoked operation was the basis for later models. The research [1] was based on the single shock wave model of Schwenk et al. [2] and prior experimental research by Miller and Hartmann [3]. The latter relied on a study of shock wave detachment by Moeckel [4] and total pressure loss in cascade shock systems by Klapproth [5]. The basic approach was improved by Bloch et al. [6]. Although this model can be used for a broader range of inlet angles, it considers only unchoked operation. The approach of Schoeiri [7] includes the influence of oblique shocks by modifying the diffusion factor. However, it is applicable only for sharp airfoils operating with attached shocks. More recent models consider a wider area of operation. Boyer and O'Brien [8] combined the approaches of Bloch et al. [6] and Koenig et al. [9], which was applied near the choke, and interpolation was performed between the characteristic regimes. A new chapter in shock loss modeling was introduced by papers such as

that by Aguirre et al. [10]. However, this approach is complex and insufficiently described to be applied without certain improvisations, which alter the results.

The shock loss prediction method described in this paper relies on analytical modeling using the standard relations for adiabatic compressible flows with shocks. Although the application of iterative procedures cannot be avoided entirely, numerical integration across the control volume is not used. Analytical modeling includes the auxiliary approximated corrections, obtained by means of numerical analysis of example cases.

Basic Considerations

Two basic modes of cascade operation are considered. The first is *unstarted* or *unchoked* operation (Fig. 1(a)), with a dual shock wave pattern. In a single-passage control volume, the *initial* shock wave is a detached bow shock, followed by the *passage shock*, generally a normal or strong oblique shock wave, resulting in a subsonic outflow. The *started* or *choked* operation (Fig. 1(b)) occurs when the passage shock is split. The *first passage shock*, now effectively a weak bow shock, allows the re-establishment of the supersonic flow downstream. The *second passage shock* is located inside the blade passage and can be normal or oblique but is generally strong for the considered field of application. Although not instantly obvious, the subsonic regimes (Figs. 1(c) and 1(d)) can be treated as being analogous to the corresponding supersonic modes, excluding the initial bow shock presence.

Choking occurs when subsonic and supersonic zones become effectively separated, thus preventing upstream propagation of the pressure waves. This is usually the case when the strong passage shock is ingested in the blade passage and the effective inflow angle becomes fixed to its minimum value related to the unique incidence. An attempt additionally to lower the inflow angle will limit the axial velocity and decrease the inlet Mach number. This action is performed by the pressure increase produced by the system of repeating bow shocks or, in the subsonic case, the continuous propagation of pressure waves from the increasingly loaded suction side. The reduced inflow angle value will match the choking at now lowered Mach number.

¹Corresponding author.

Manuscript received January 17, 2022; final manuscript received February 7, 2022; published online March 4, 2022. Tech. Editor: David G. Bogard.

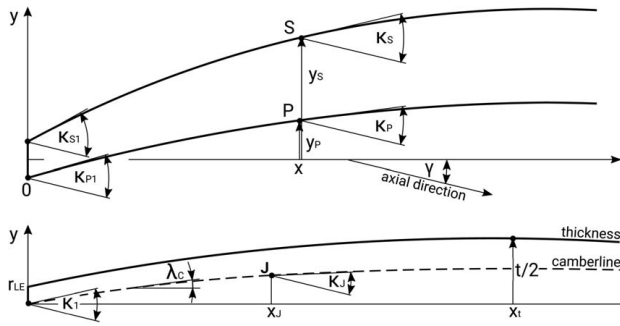


Fig. 4 Simplified blade geometry

where $R_C = R_{C1}$ and the camber line elevation is

$$y_C = -R_C + y_f \pm \sqrt{R_C^2 - (x - x_f)^2} \quad (2)$$

Here, the sign \pm is taken according to the sign of $\kappa_1 - \kappa_J$. Each arc segment has a corresponding pair of parameters y_f and x_f , and only one pair is equivalent to the real camber line and its position. The local angle of the camber line is $tg \lambda_C = y'_C(x)$.

The thickness distribution y_t is also described with two arcs joined at the position x_t where the maximum thickness t is applied. For $x < x_t$, it is

$$y_t = -R_t + \frac{t}{2} + \sqrt{R_t^2 - (x - x_t)^2}, \quad R_t = \frac{x_t^2 + d^2}{2d} \quad (3)$$

where the radius R_t is calculated using $d = t/2 - r_{LE}$. Since the large curvature of the blade in the leading-edge region slows certain calculation procedures, the leading edge is placed at $x=0$ and treated as a singularity (Fig. 4). The local suction/pressure side elevation $y_{S/P}$ and angle $\kappa_{S/P}$ are

$$y_{S/P} = y_C \pm y_t \cos \lambda_C \quad (4)$$

$$\kappa_{S/P} = \arctg(y'_C \pm y'_t \cos \lambda_C) + \gamma \quad (5)$$

For example, the suction side inlet angle $\kappa_{S1} = \kappa_S(x=0)$ corresponds to the point that, in real geometry, connects the leading edge with the rest of the suction side. The leading-edge angle distribution $\kappa_1 - 90 \text{ deg} < \kappa_S < \kappa_{S1}$ is concentrated at $x=0$. Similarly, the angle κ_{S2} is located at $x=1$.

For DCA and NACA65 airfoils, the appropriate location of maximum thickness x_t is used with $\gamma = (\kappa_1 + \kappa_2)/2$ and $\kappa_J = \gamma$. For MCA airfoils, as specified in test cases [12,13], parameters x_t , κ_J , and γ are additional inputs.

The inlet suction side turning angle ϵ is

$$\epsilon = \kappa_{S1} - \kappa_{Sk}, \quad \kappa_{Sk} = \kappa_S(x_k) \quad (6)$$

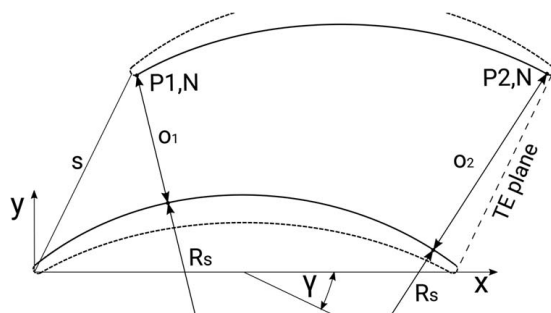


Fig. 5 Inlet and outlet openings for DCA cascades

Inlet and Outlet Openings

Inlet and outlet openings need to be determined using a precise geometry description that considers all relevant leading-edge details. Iterative calculations usually needed for such an approach can be avoided by employing the DCA geometry model of Fellerhoff [14]. It is used to determine the suction side radius R_S and the center point (x_{S0}, y_{S0}) , together with the exact location of the point P1 for the nearby profile N (Fig. 5). The inlet opening is

$$o_1 = \sqrt{(x_{P1,N} - x_{S0})^2 + (y_{P1,N} - y_{S0})^2} - R_S \quad (7)$$

The results are shown in Fig. 6. Similarly, the outlet opening o_2 is determined for the point P2, N of the adjacent profile and additionally compared with the opening at the trailing edge plane.

For MCA airfoils, a simple modification of the model [14] collocates the maximum camber, maximum thickness, and junction point, where κ_J is taken to be equal to γ . Since such an equivalent geometry generally differs from the real MCA profile, the computed opening o_1 must be corrected as $o_1 := o_1 + \Delta y_S$. Here, Δy_S is the difference between $y_S(x_k)$ according to Eq. (4) for the equivalent geometry and for the real MCA shape. To check whether internal contraction occurs, the blade passage openings at the position of the maximum thickness x_t and $x_t + x_k$ must be estimated. The openings obtained are then corrected by the appropriate values of Δy_S and Δy_P . The minimum value $\min[o(x_t), o(x_t + x_k)]$ represents the opening related to the maximum thickness position o_t .

For NACA65 airfoils, the inlet and outlet openings are determined according to Aungier [15].

Flow Exit Angle and Critical Mach Number

The cascade outlet angle $\beta_2 = \beta_{ij}$, used to determine the outlet Mach number, is an externally provided input. The reference outflow angle is determined using Ref. [16] for NACA65 and DCA airfoils and Ref. [17] for MCA blades, whereas the off-design deviation model uses curves based on results obtained by MISES [18]. The critical Mach number M_1^{cr} is determined as in Ref. [19], using the input from Ref. [20] and applying the additional correction as in Ref. [9].

Relations for Compressible Flow

Shock waves are modeled applying the oblique shock relations, including the normal shock as a special case. The local Mach number behind a shock wave M'' is found as

$$M'' = M''(\theta, \delta, M') \equiv M''(\theta, M') \quad (\delta = \delta(\theta, M')) \quad (8)$$

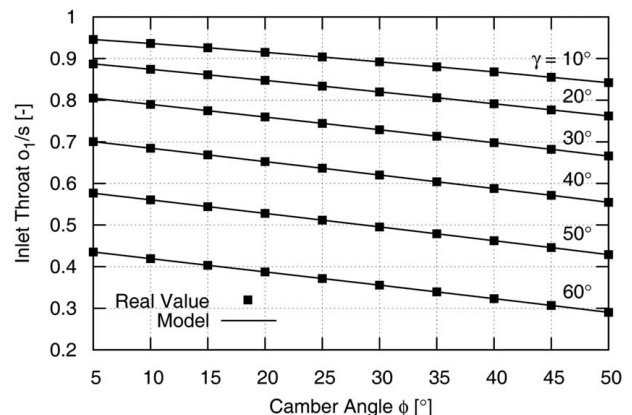


Fig. 6 Evaluation of the inlet throat for DCA cascades

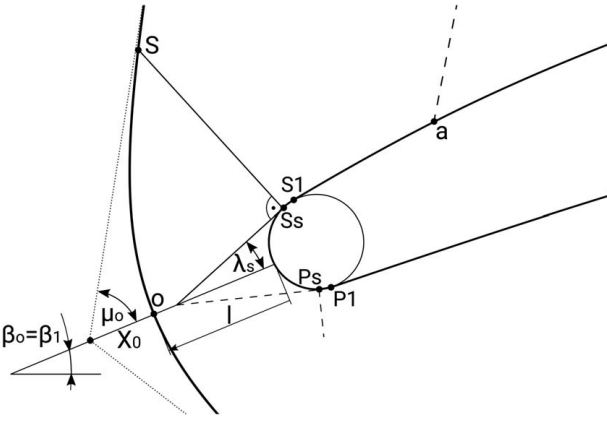


Fig. 7 Configuration of the detached bow shock

where δ is the deflection angle and θ is the shock angle relative to the inflow direction. These widely known relations can be found in the literature, e.g., Ref. [21], and are given in Appendix C.

Prandtl–Meyer expansion or compression is determined from the change of the Prandtl–Meyer angle ν :

$$\nu_2 + \beta_2 = \nu_1 + \beta_1, \quad \rightarrow \quad \Delta\nu = \beta_1 - \beta_2 \quad (9)$$

according to given flow angles β_1 and β_2 . Using the well-known Prandtl–Meyer function $\nu = \nu(M)$ and its inverse form $M = M(\nu)$, the resulting Mach number is found as $M_2 = M(\Delta\nu, M_1)$. The approximate inverse Prandtl–Meyer function of Hall [22] is given in Appendix D.

When the isentropic process is modeled as an idealized nozzle flow, the applied relations are

$$a = \frac{A}{A_s} = a(M), \quad \rightarrow \quad \frac{A_2}{A_1} = \frac{A_2/A_s}{A_1/A_s} = \frac{a(M_2)}{a(M_1)} \quad (10)$$

where $a \geq 1$ is the ratio between the flow area A corresponding to a local Mach number M and the area A_s related to sonic conditions $M_s = 1$. The final Mach number M_2 is determined using

$$a(M_2) = \frac{A_2}{A_1} a(M_1) \quad (11)$$

and applying the inverse function $M_2 = M(a_2)$. The approximated inverse function $a(M)$ is given in Appendix E.

Bow Shock Parameters

The hyperbolic representation of a bow shock from Ref. [4] is shown in Fig. 7. The detachment length is l and X_0 represents an additional distance from the vertex to the asymptote center. The central subsonic zone formed behind the mean part of the bow shock is ended downstream with the occurrence of the first sonic Mach wave \overline{SSs} , which extends from the body sonic point, in this case the suction side sonic point Ss . The slope of the sonic Mach wave \overline{SSs} is λ_s and it is orthogonal to the suction side contour in Ss . The angle λ_s is a function of the inlet Mach number $M_o = M_1$, and X_0 and l additionally depend on the leading-edge radius r_{LE} . These relations are explained in Appendix B.

Choke Angle

The choke angle corresponds to the inlet Mach number M_1 and is determined using the modified model of Schnoes [23]. For the subsonic inflow, it is based on the continuity approach of Cumpsty [24], where the choke angle is calculated as

$$\beta_1^{\text{ch}} = \arccos\left[\left(\frac{o}{s}\right)a(M_1)\right] + K_M \cdot \Delta\beta_s, \quad M_1 \leq 1 \quad (12)$$

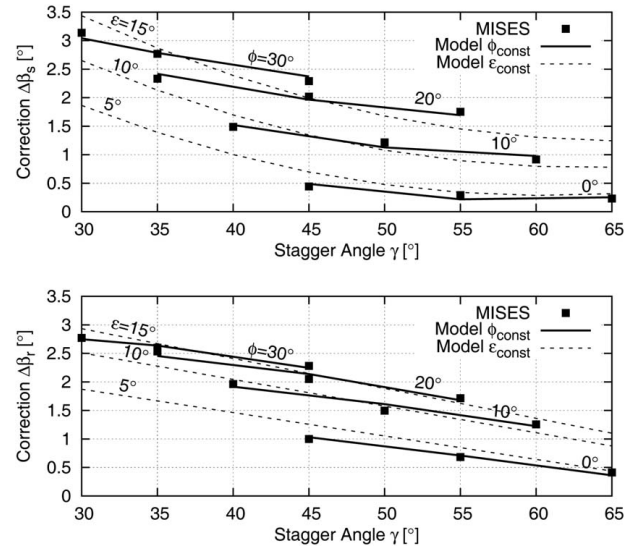


Fig. 8 Variations of $\Delta\beta_s$ and $\Delta\beta_r$ with parameters ϕ and γ for DCA profiles. The blade maximum thickness t/c varies linearly from 0.03 to 0.075 as the camber angle ϕ is increased

The ratio o/s is determined according to the minimum opening, i.e., throat $o := \min(o_1, o_2, o_r)$.

For the supersonic inflow, the choke angle is

$$\beta_1^{\text{ch}} = \arccos\left(\frac{o}{s}\right) + Q_M \cdot \Delta\beta_r + \Delta\beta_s, \quad M_1 > 1 \quad (13)$$

The sonic and reference supersonic choke angle corrections, $\Delta\beta_s$ and $\Delta\beta_r$, respectively, are multiplied by linear coefficients

$$K_M = \frac{M_1 - M_1^{\text{cr}}}{1 - M_1^{\text{cr}}}, \quad Q_M = \frac{M_1 - 1}{M_1^{\text{cr}} - 1} \quad (14)$$

The corrections $\Delta\beta_s$ and $\Delta\beta_r$ encompass the effects of shock-related, non-isentropic phenomena that occur upstream of the passage inlet and additionally increase the choke angle β_1^{ch} compared with the ideal value $\arccos(o/s)$. They were determined using MISES calculations for a set of DCA cascades with different camber and stagger angles, ϕ and γ , respectively.

For each case, $\Delta\beta_s$ was determined as the difference between the MISES-computed choke angle for $M_1 = 1$ and the o/s related value. However, since the discussed flow effects are mostly related to the inlet suction side turning ϵ , a data fit was performed as a function of ϵ and stagger γ (Fig. 8):

$$\Delta\beta_s = 5.4050 + 0.2120|\epsilon| - 0.1945\gamma - 0.001833|\epsilon| \cdot \gamma + 0.001678\gamma^2 \quad (15)$$

Correction $\Delta\beta_r$ was determined using the differences between the MISES choke angle for the reference Mach number $M_1^{\text{cr}} = 1.2$ and for the sonic inflow $M_1 = 1$. The fitted function is

$$\Delta\beta_r = 2.079 + 0.22261|\epsilon| - 0.03531\gamma - 0.004292\epsilon^2 - 0.001138|\epsilon| \cdot \gamma \quad (16)$$

Both corrections must be limited as $\Delta\beta_s, \Delta\beta_r \geq 0$.

Critical Mach Number Correction

When Eq. (12) is inversely solved applying the inflow angle β_1 , the solution represents the choking Mach number M_1^{ch} . It is used to re-evaluate the critical Mach number M_1^{cr} . The value $M_1^{\text{ch}} - 0.15$ is compared with the estimate of Ref. [9] and the minimum is selected.

This step is performed to avoid the paradoxical situation $M_1^{cr} \geq M_1^{ch}$, which can occur in some instances. The re-evaluation is done before the choke angle is computed.

Unchoked Operation

This mode of operation occurs when the inflow angle exceeds the choking angle $\beta_1 > \beta_1^{ch}$ and, for now, only the supersonic operation $M_1 \geq 1$ is considered. The steps needed to determine such an operation mode are given below.

Point o. The initial shock wave parameters are determined for $M_o = M_1$ using equations from Appendix B. The tangential angle κ_{Ss} at the suction side sonic point Ss is determined using λ_s as

$$\kappa_{Ss} = \beta_o + \lambda_s \quad (\beta_o = \beta_1) \quad (17)$$

Point a is defined over the Mach wave \overline{ab} . This point can be located at the leading edge or at the following part of the suction side contour. Since the simplified blade geometry (Fig. 4) places the leading edge in the singular position $x = 0$, two separate procedures are used to determine Mach angle μ_a .

The limiting case occurs when point a is located in $S1$, which connects the leading edge and the following suction side arc and is placed at $x = 0$ in the simplified geometry model. Then, the expansion from Ss to $a \equiv S1$ is calculated as

$$M_{S1} = M(\Delta\nu, M_{Ss}), \quad \Delta\nu = \kappa_{Ss} - \kappa_{S1} \quad (18)$$

The related Mach angle μ_{S1} and the limiting value μ_{lim} are

$$\mu_{S1} = \arcsin \frac{1}{M_{S1}}, \quad \mu_{lim} = \arctg \left[\frac{g - y_{S1}}{x_k - l} \right] + \gamma - \kappa_{S1} \quad (19)$$

If the condition $\mu_{S1} \geq \mu_{lim}$ is true, then point a is located behind $S1$. The value $x_a > 0$ is determined by iterative computation of the suction side angle κ_{Sa} and elevation y_{Sa} :

$$\kappa_{Sa} = \kappa(x_a), \quad y_{Sa} = y(x_a) \quad (20)$$

The new position x_a^n is found as follows:

$$\Delta\nu = \kappa_{Ss} - \kappa_{Sa}, \quad M_a = M(\Delta\nu, M_{Ss}), \quad \mu_a = \arcsin \frac{1}{M_a} \quad (21)$$

$$x_a^n = x_k - l - (g - y_{Sa}) \cdot \tg[\gamma - \kappa_{Sa} - \mu_a + 90 \text{ deg}] \quad (22)$$

The relaxation of 0.1 is applied to determine the new location x_a^n , while the initial position is taken as $x_k - l$. The limitations $\Delta\nu \geq 0$ and $x_a^n \geq 0$ are performed in each iteration.

If, however, the condition $\mu_{S1} < \mu_{lim}$ is satisfied, point a is located at the leading-edge singularity $x_a = 0$. The initial guess $M_a = M_{S1}$ is applied to an iterative procedure that includes

$$\Delta\nu = \Delta\nu(M_{Ss}, M_a), \quad \kappa_{Sa} = \kappa_{Ss} - \Delta\nu \quad (23)$$

$$\mu_a = \arctg \left[\frac{g - y_{S1}}{x_k - l} \right] + \gamma - \kappa_{Sa}, \quad M_a^n = \frac{1}{\sin \mu_a} \quad (24)$$

The relaxation factor used for the calculation of M_a^n is 0.5.

The previous considerations are valid only if the sonic point Ss is placed on the leading edge. However, if the condition $\kappa_{Ss} < \kappa_{S1}$ is true, then the point Ss is located behind $S1$, and the procedure for $x_a > 0$ must be applied. In an extreme case, the sonic point Ss is located far downstream, behind the first possible Mach wave position $M_a = 1$. This is checked by solving Eqs. (20) and (22) for values $M_a = 1$ and $\mu_a = 90 \text{ deg}$. If the condition $\kappa_{Ss} < \kappa_{Sa}$ is true, then the Mach wave \overline{ab} is treated as sonic $\kappa_{Ss} = \kappa_{Sa}$.

Point b. The local Mach number behind the shock wave is

$$M_b'' = M''(\theta_b, M_b), \quad \theta_b = 90 \text{ deg}, \quad M_b = M_a \quad (25)$$

and the reference inflow angle is $\beta_b = \beta_d = \kappa_{Sa}$. Thus far, all computations were performed applying the detachment parameters related to M_o . This produces good results and avoids excessive iteration. However, since the position of point d is crucial, the further procedure will employ the detachment re-evaluated for M_b . As the basic model of Moeckel [4] considers a single body, the detachment parameters y_s , X_0 , and l become underpredicted when the cascade solidity decreases. Therefore, a correction for this effect was made and the equations are given in Appendix F.

Point d. At the suction side, Prandtl–Meyer expansion continues until point d is reached. Its position is calculated iteratively as

$$x_d = x_k - l + (g - y_{Sd}) \cdot \tg[90 \text{ deg} - \gamma - \theta_b + \bar{\beta}_{bd}] \quad (26)$$

When the camber angle increases, the pitch-wise pressure gradient deforms the shock wave which becomes *s-shaped* (Fig. 9) as it aligns to be normal to the flow locally. The averaged flow angle $\bar{\beta}_{bd}$ should be taken as

$$\bar{\beta}_{bd} = (\beta_b + \beta_d)/2, \quad \beta_d = \kappa_{Sd} \quad (27)$$

Each iteration demands a re-evaluation of y_{Sd} and κ_{Sd} according to the new value of x_d .

The Mach number M_d results from Prandtl–Meyer expansion from Ss to d . The shock wave inclination angle in d is relative to the local inflow:

$$\theta_d = \theta_b - (\beta_b - \beta_d) = \theta_b - (\kappa_{Sa} - \kappa_{Sd}) \quad (28)$$

Now the Mach number behind the shock M_d'' can be evaluated.

Planes b–d. The flow behind the shock wave \overline{bd} is subsonic and the representative Mach number is

$$M_{bd}'' = (M_b'' + M_d'')/2 \quad (29)$$

Planes i–j. The Mach number at exit station \overline{ij} is determined directly from M_{bd}'' and α_1 , for the given outflow angle β_2 :

$$M_{ij} = M(\alpha_{ij}), \quad \alpha_{ij} = a(M_{ij}) = \frac{s \cdot \cos \beta_2}{\alpha_1} a(M_{bd}'') \quad (30)$$

It could be argued that the existence of internal contraction behind the passage shock would require an additional check if the flow is choked in α_r . However, this was already taken into account with the condition $\beta_1 > \beta_1^{ch}$.

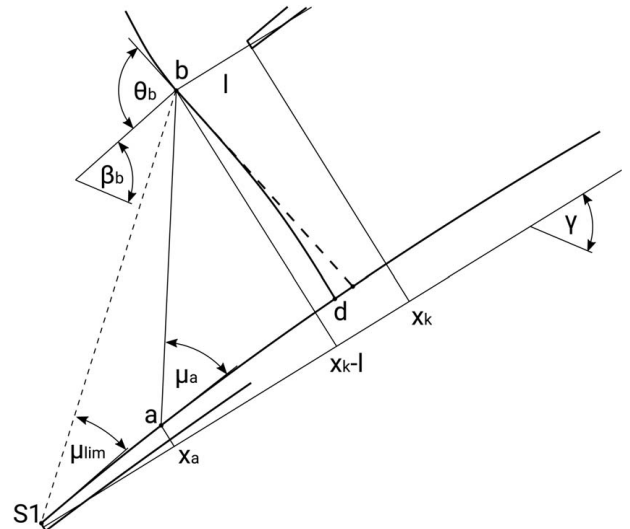


Fig. 9 Unchoked flow model

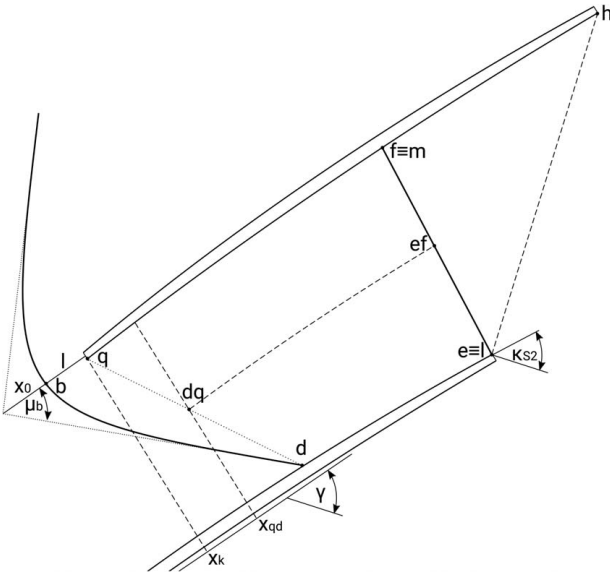


Fig. 10 Choked flow model

Choked Operation

If the input value of β_1 is lower than the choking limit, it must be bounded to $\beta_1 := \beta_1^{\text{ch}}$ and the operation is considered to be choked. Again, the case of supersonic inlet $M_1 \geq 1$ is discussed, and parameters related to points o , a , and b are determined as for the unchoked operation. However, the shock wave bd is now effectively a weak bow shock, and the supersonic flow is established downstream. Although the shock is strong in the proximity of vertex b , the flow is re-accelerated back to supersonic downstream due to finite blade thickness.

Point d. The location of this point is determined as

$$x_d = x_k - l - X_0 + g \cdot tg[90 \text{ deg} - \gamma - \mu_b + \beta_b] \quad (31)$$

and is limited between $x_k - l$ and $x_l = 1$ (Fig. 10). The member related to y_{sd} is disregarded to avoid iterative calculation since it does not influence the solution significantly. Once x_d and related κ_{sd} are known, the Mach number M_d is obtained for the Prandtl–Meyer expansion from κ_{ss} to κ_{sd} . The local shock wave inclination angle is

$$\theta_d = \theta|_{y=g} - (\beta_b - \beta_d) \quad (32)$$

and $\theta(y)$ can be found in Appendix B as given by Moeckel [4]. The minimum value of θ_d must be bounded to $\mu_d = \arcsin(1/M_d)$.

Finally, the Mach number behind the shock wave M_d' can be computed from θ_d and M_d .

Point q represents a pressure side location where the supersonic flow has been fully re-established. This occurs due to the expansion from the pressure side sonic point P_s to the vertex P_1 (Fig. 7). The latter lies at the end of the leading edge, thus ending the convex part of the pressure side:

$$M_q = M''(\Delta\nu, M_{Ps}), \quad \Delta\nu = \kappa_{P1} - \kappa_{Ps} = \kappa_{P1} - (\beta_b - \lambda_s) \quad (33)$$

It should be noted that $\Delta\nu$ is again limited to $\Delta\nu \geq 0$.

Planes d–q. The representative Mach number M_{dq} is calculated and limited as

$$M_{dq} = (M_d'' + M_q)/2, \quad M_{dq} \geq 1 \quad (34)$$

Although internal, the passage flow is here treated using Prandtl–Meyer expansion. The fictive mean line position x_{dq} allows the calculation of representative suction side angle κ_{sdq} :

$$\kappa_{sdq} = \kappa_s(x_{dq}), \quad x_{dq} = (x_k + x_d)/2 \quad (35)$$

Planes e–f. The passage expansion ends with the normal shock \overline{ef} , which is in the reference case placed at the location of the outlet opening \overline{lm} . As mentioned, the expansion between the fictive plane \overline{dq} and the shock \overline{ef} is determined by applying the Prandtl–Meyer relations:

$$M_{ef} = M(\Delta\nu, M_{dq}), \quad \Delta\nu = \kappa_{sdq} - \kappa_{s2} \quad (36)$$

For the blades with negative pressure side camber angle ϕ_P , internal compression occurs instead of expansion, and negative $\Delta\nu$ must be bounded to satisfy $M_{ef} \geq 1$. The Mach number behind the shock M_{ef}' is computed using the normal shock relations.

Intersection with b–d. If the unbounded position x_d is ≥ 1 , then two passage shocks are intersected. The length of the merged part of the shock used in the following section is

$$\Delta y_M = (x_d - 1) \cdot tg[\gamma + \mu_b - \beta_b] \quad (37)$$

Planes i–j. The exit plane Mach number M_{ij} is found for isentropic flow between stations $\overline{ef} \equiv \overline{lm}$ and \overline{ij} . The related flow areas are o_2 and $s\cos\beta_2$, respectively.

Choked Operation With Oblique Second Passage Shock

In some instances, it is necessary to analyze an additional mode of choked operation where shock \overline{ef} is placed in \overline{lh} (Fig. 10). The flow now experiences additional Prandtl–Meyer expansion driven by the curvature of the trailing edge, where the expansion angle is $\Delta\nu = \kappa_{s2} - 0 \text{ deg}$. The shock wave \overline{ef} is now computed as an oblique shock with the inclination $\theta_{lh} = 90 \text{ deg} - \beta_2$. The exit Mach number M_{ij} is determined using isentropic nozzle flow relations for the flow between sections with areas $(s + o_2)/2$ and $s\cos\beta_2$.

Total Pressure Ratio

The overall value of the total pressure ratio Π_{12} is calculated using elementary ratios Π_o , Π_{bd} , and Π_{ef} :

$$\Pi_{12} = p_o^0 / p_1^0 = \Pi_o \cdot \Pi_{bd} \cdot \Pi_{ef} \quad (38)$$

The member Π_o is determined considering the repetitive shock structure as in Klapproth [5]. However, since the bow shock quickly weakens, the finite span of integration $[0, 2y_s]$ is used. The integration is done employing the trapezoid rule for the points $y = 0$, y_s and $2y_s$ as

$$\Pi_o = 1 - \frac{y_s}{g} \left[2 - \frac{\Pi_0}{2} - \Pi_{y_s} - \frac{\Pi_{2y_s}}{2} \right] \quad (39)$$

The local pressure ratios are determined with oblique shock relations from Ref. [5] and the expression $\theta(y)$ from Appendix B and the Mach number M_b is applied in all related equations:

$$\Pi_0 = \Pi(\theta_0, M_b), \quad \Pi_{y_s} = \Pi(\theta_{y_s}, M_b), \quad \Pi_g = \Pi(\theta_d, M_b) \quad (40)$$

Unchoked operation. The representative pressure ratio of the passage shock is computed as

$$\Pi_{bd} = (\Pi_b + \Pi_d)/2 \quad (41)$$

employing the known Mach numbers M_b and M_d and inclination angles θ_b and θ_d . In this mode, the second passage shock does not exist, i.e., $\Pi_{ef} = 1$.

Choked operation. Parameter Π_{bd} is now determined as

$$\Pi_{bd} = \frac{1}{g} \left[y_s \frac{\Pi_0 + \Pi_{y_s}}{2} + (g - y_s) \frac{\Pi_{y_s} + \Pi_g}{2} \right] \quad (42)$$

where y_s must be limited to g . Local pressure ratios are

$$\Pi_0 = \Pi(\theta_0, M_b), \quad \Pi_{y_s} = \Pi(\theta_{y_s}, \approx M_b), \quad \Pi_g = \Pi(\theta_d, M_d) \quad (43)$$

Local inclination angles, θ_0 and θ_{ys} , are determined as $\theta = \theta(y)$, while θ_d is known from Eq. (32).

The shock wave \overline{ef} is treated as a one-dimensional normal shock:

$$\Pi_{ef} = \Pi(\theta = 90 \text{ deg}, M_{ef}) \quad (44)$$

If the first and second passage shocks intersect, the local total pressure ratio at the merged part is $\Pi_M = \Pi(90 \text{ deg}, M_d)$. The overall total pressure ratio corrected for this value is then

$$\Pi_{12} := \Pi_{12} + \frac{\Delta y_M}{g} \Pi_{o,0} (\Pi_M - \Pi_{bd,g} \cdot \Pi_{ef}) \quad (45)$$

The length of the merged shock part Δy_M is calculated using Eq. (37). The pressure ratio $\Pi_{o,0}$ is obtained from Eq. (40), and $\Pi_{bd,g}$ is the corresponding value from Eq. (43).

Exit Static Pressure

The exit Mach number $M_2 = M_{ij}$ is needed to determine the normalized exit static pressure:

$$\frac{p_{ij}}{p_o} = \Pi_{12} \left(\frac{p}{p_o} \right)_{ij}, \quad \left(\frac{p}{p_o} \right)_{ij} = \left(1 + \frac{\kappa - 1}{2} M_{ij}^2 \right)^{-\kappa/(\kappa-1)} \quad (46)$$

This is only relevant in the case of the choked flow.

Total Pressure Loss Coefficient

The total pressure loss coefficient is computed as

$$\varpi = \frac{1 - \Pi_{12}}{1 - (p/p_o)_o} \quad (47)$$

where $(p/p_o)_o$ is obtained from the right expression in Eq. (46) for input $M_o = M_1$.

Unchoked operation. For $\beta_1 > \beta_1^{\text{ch}}$, the total pressure loss ϖ is simply calculated by applying Eq. (47).

Choked operation. Here, the loss coefficient ϖ additionally depends on the input value of the exit pressure p_2 . First, the unchoked model is used for $\beta_1 = \beta_1^{\text{ch}}$ to determine the magnitude of the corresponding unchoked loss ϖ_U . Then, the loss ϖ_{CN} is determined for the case of choked operation with the normal passage shock \overline{ef} located in \overline{lm} . The resulting total pressure loss is interpolated as

$$\varpi = \varpi_{CN} + \frac{p_2 - p_{CN}}{p_{CN} - p_U} (\varpi_{CN} - \varpi_U) \quad (48)$$

The (normalized) pressure values p_U and p_{CN} correspond to p_{ij} determined from Eq. (46), for the given cases.

If the value of p_2 is lower than p_{CN} , the total pressure loss ϖ is interpolated between cases CN and CO , where the latter refers to the reference case of choked operation with an oblique second

passage shock placed in \overline{lh} . If the pressure p_2 is higher than p_U , the total pressure loss ϖ is taken as ϖ_U .

Operation With Subsonic Inlet

When subsonic but supersonic inflow $M_1^{\text{cr}} < M_1 < 1$ is experienced, the supersonic procedure is applied with the following modifications. Initially, the detachment parameters at point o and the position of point a are determined for the input value $M_o = 1$. The sonic point Ss is then relocated downstream through the correction of the reference angle $\Delta\nu = \kappa_{Ss} - \kappa_{Sa}$ as

$$\Delta\nu = K_M \cdot \Delta\nu_{M=1}, \quad K_M = \frac{M_1 - M_1^{\text{cr}}}{1 - M_1^{\text{cr}}} \quad (49)$$

For unchoked flow, the expansion angle from Ss to d is corrected in the same manner: $\Delta\nu = K_M \cdot \Delta\nu_{M=1}$.

However, for choked operation, the considered expansion angle from Ss to d is revised as

$$\Delta\nu = K_M \cdot \Delta\nu_U + (\Delta\nu_C - \Delta\nu_U) \quad (50)$$

where $\Delta\nu_U$ and $\Delta\nu_C$ are uncorrected expansion angles from Ss to d for the unchoked and choked regimes, respectively, determined for $M_o = 1$. Although the initial shock detachment parameters have been computed to obtain the position of the sonic point Ss , the initial bow shock is not considered when estimating the related total pressure drop, i.e., $\Pi_o = 1$. All subsequent parts of the procedure remain unchanged.

Airfoils With Negative Camber

The unchoked operation of blades with negative camber (Fig. 11(a)) is equivalent to the operation mode shown in Fig. 1(a). When the inlet flow angle β_1 decreases, the flow behind bd can be re-accelerated along the unguided part of the convex lower side to form a supersonic zone (Fig. 11(b)). This zone is terminated with a normal shock located near the trailing edge. The length of this shock quickly outgrows the single pitch, increasing the losses. If the angle β_1 is reduced further, the shock becomes more inclined, and the front boundary of the supersonic domain moves upstream. Choking occurs when this boundary encounters the outlet opening, effectively closing it. From this point, the flow on both sides of the trailing edge is supersonic (Fig. 11(c)). The flow angle value $\beta_1 = \beta_1^{\text{ch}}$ is now fixed and the loss is determined by the exit static pressure.

A precise method to predict the transition between the modes was not established, and all are modeled using the configuration in Fig. 11(c). Relevant points h and l represent the lower and upper trailing edge vertices, respectively (Fig. 2). The trailing edge shock (Fig. 11(c)) in the proximity of the lower side produces the Mach number M_h'' . At the same time, this value corresponds to M_l related to the last Mach wave from the expansion fan. This fan dictates the first part of the lower side expansion, while the

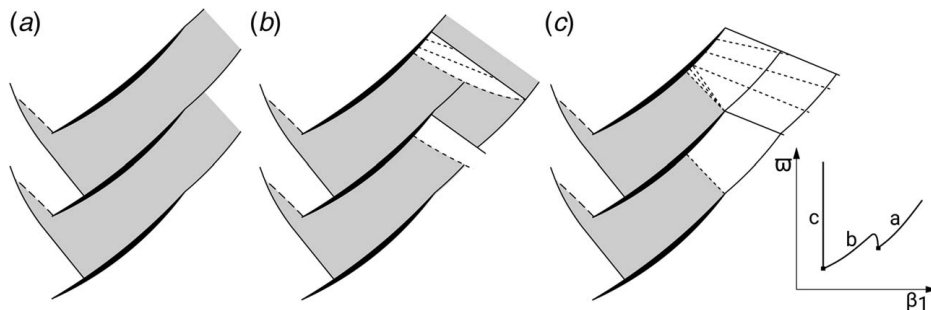


Fig. 11 Operational modes for a cascade of airfoils with negative camber: (a) unchoked, (b) unchoked with trailing edge shock, and (c) fully choked

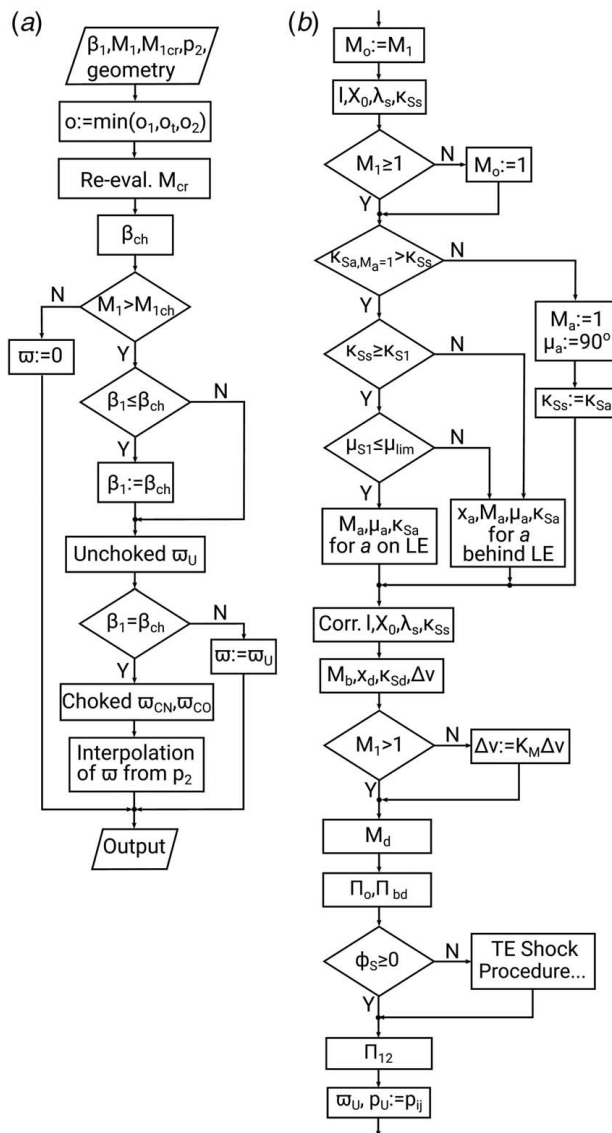


Fig. 12 Flowcharts of the present model: (a) basic structure and (b) unchoked mode procedure

remaining part is led by the curvature of the lower side itself, determining M_h' . The system is closed when the inclination angle of the trailing edge shock θ_h is specified. For the choking point, θ_h is set to be equal to the value $\theta_{lim}(M_h')$ that produces $M_h'' = 1$. This approach is applied for unchoked regimes in Figs. 11(a) and 11(b). For the choked branch of the loss curve $\beta_1 = \beta_1^{ch}$, interpolation is used. An arbitrary reference operating point is calculated analogously for $\theta_h = \theta_{lim} - 8$ deg. Since the front of the trailing edge shock wave has outgrown the single pitch, its repetitive structure cannot be disregarded and four positions, namely, $y = 0, g, 2g, 3g$, are used to compute Π_h and the exit static pressure. As it was planned to extend the model to turbine cascades, details will be discussed in subsequent papers.

Even more complicated flow patterns occur for low-cambered airfoils where both the lower and upper sides are convex. Here, the choked mode resembles the configuration in Fig. 1(b), with the added trailing edge shock waves and expansion fans that place the now unbounded normal shock behind the outlet opening. Since this normal shock is dominant, these cascades are treated by employing the main model for positive cambered blades (Fig. 1). Therefore, the negative camber model is used

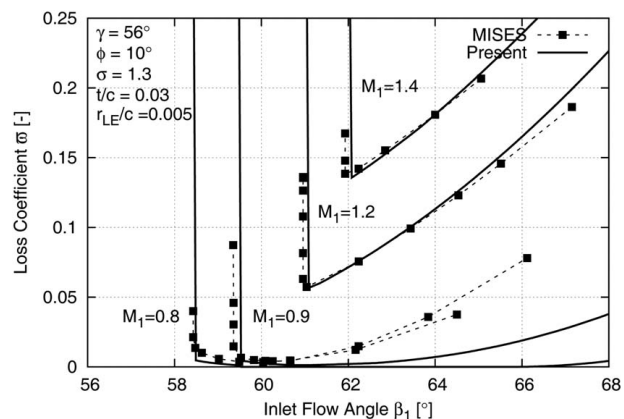


Fig. 13 Shock loss curves for MCA cascade

Table 1 Computed Mach numbers for an MCA cascade with parameters $\gamma = 56$ deg, $\phi = 10$ deg, and $\sigma = 1.3$; the inlet flow angle is $\beta_1 = 63.7$ deg

	M_1	$M_b = M_a$	M_d	M_d''	M_{ij}
MISES	1.2	1.34	1.42	0.70	0.55
Model	1.2	1.36	1.47	0.72	0.56

only for airfoils with $\phi_S < 0$ deg. The cases with internal contraction $\alpha_1 < \alpha_1 < \alpha_2$ are also treated as positive cambered airfoils.

Implementation

Implementation includes approximately 2000 computer code lines, excluding the external procedures for reference flow angle deviation, critical Mach number, and others. The basic flowchart is shown in Fig. 12(a) and an unchoked procedure is explained in Fig. 12(b). When all internal computation steps are carried out according to aforementioned limitations, the code operates stably for a wide variety of input parameters.

The implementation includes additional features such as the loss curve rounding in the vicinity of the choking point. The width of the rounded part is estimated according to M_1 and $\kappa_1 - \gamma$. The related loss increase is accomplished by adding a small local shock wave on the pressure side behind the leading edge. As the occurrence of this phenomenon is not based on precise physical modeling, it is not described here.

Validation

The present shock loss model was validated with a number of two-dimensional cascade flows previously computed by MISES in the inviscid mode. If the effect of numerical artificial viscosity in MISES is disregarded, both approaches consider only losses directly produced by shocks.

The first case considered is a transonic cascade with high-stagger, low-camber MCA airfoils, typical for the tip section of a transonic rotor. The maximum camber and thickness are placed at 60% of the chord and the junction tangent is parallel to the chord, $\kappa_j = \gamma$. Other geometry parameters are given in Fig. 13, where the loss curves are compared. It can be seen that the agreement is good for supersonic inflow, whereas it is underpredicted for subsonic cases. This is due to linear interpolation of the coefficient K_M , which may not be suitable for higher values of β_1 , but produces good results when applied in throughflow. The Mach number values for a single inflow angle are compared in Table 1. The influence of the camber angle ϕ on the performance prediction was tested using

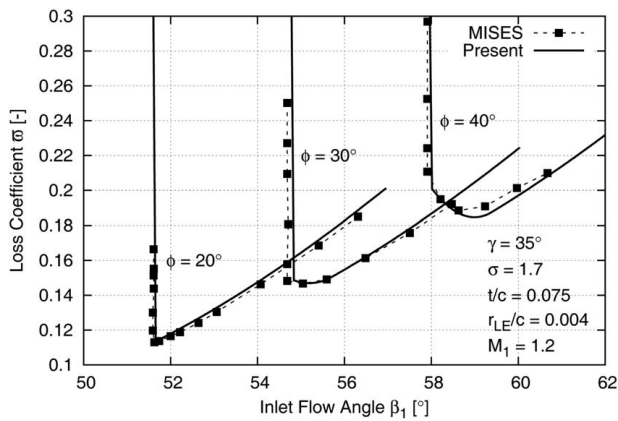


Fig. 14 Shock loss curves for DCA cascades

Table 2 Computed Mach numbers for a DCA cascade with parameters $\gamma = 35$ deg, $\phi = 30$ deg, and $\sigma = 1.7$; the inlet flow angle is $\beta_1 = 57.7$ deg

	M_1	$M_b = M_d$	M_d	M_d''	M_{ij}
MISES	1.2	1.38	1.71	0.60	0.48
Model	1.2	1.37	1.79	0.70	0.44

three high-camber and high-solidity DCA cascades. Similar configurations are used for lower sections of transonic rotors. The results are shown in Fig. 14, and a comparison of Mach numbers is given in Table 2. As can be seen, the agreement is good.

The following case considers a low-speed NACA65 cascade operating with a subsonic, yet supercritical and sonic inlet. Computed loss curves for these medium thickness airfoils are shown in Fig. 15. In contrast to the case shown in Fig. 13, the linear interpolation of K_M gives reasonably good results for the considered range of inlet flow angles.

Figure 16 shows the results for three sections of NASA Rotor 37 [12]. The airfoil geometry deviates from the equivalent MCA description with $\kappa_J = \gamma$, used to estimate the basic size of the throat. Regardless of the additional correction of the throat, a certain difference in choke angle for the hub and mid region occurs. In both cases, the difference is less than 1 deg. The underprediction of tip section losses for high values of the inflow angle β_1 is related to the occurrence of an additional oblique shock placed on the suction side, close to the leading edge. Although localized and weak, this shock produces slightly higher losses than the present model predicts.

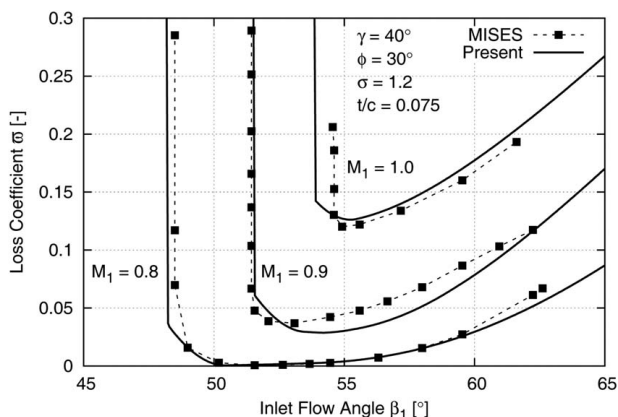


Fig. 15 Shock loss curves for NACA65 cascade

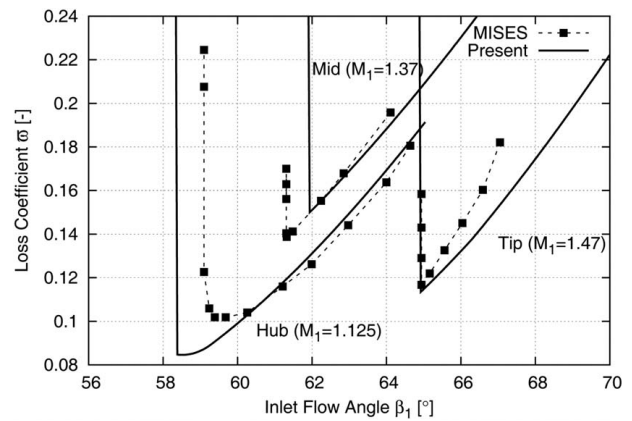


Fig. 16 Shock loss curves for rotor 37 hub, mid and tip sections

The prediction of losses for negative camber internal compression DCA cascade is shown in the example in Fig. 17.

Figures 13–17 do not show the relation between the loss and the exit static pressure for choked operation. Such a relation is given in Fig. 18. It can be seen that the agreement is relatively good for the low-cambered cascade in Fig. 13, whereas deviates for the highly cambered airfoils considered in Fig. 14. The reason for this is that for highly cambered cascades, the second passage shock becomes inclined as it is moved towards the outlet opening with the decrease in the exit static pressure. The attempts made to include this

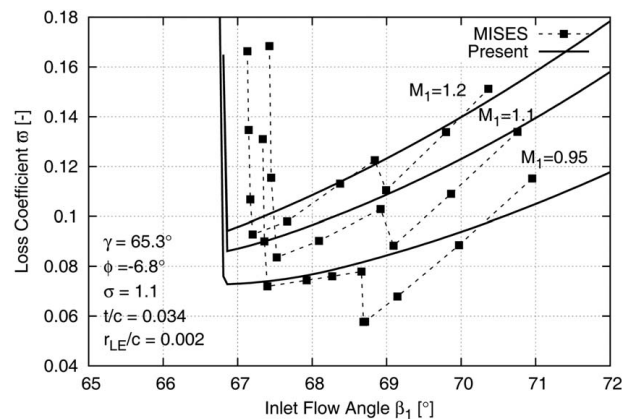


Fig. 17 Shock loss curves for a negative camber DCA cascade

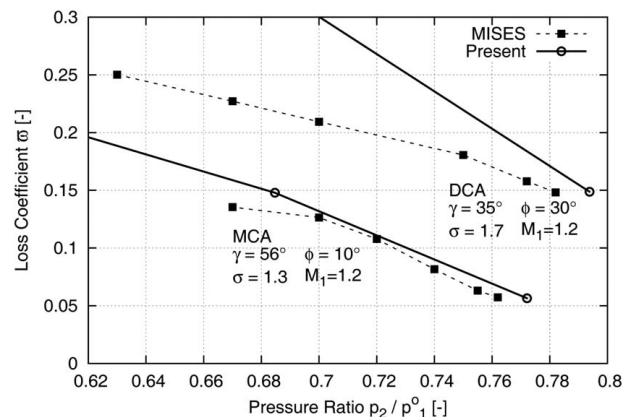


Fig. 18 Variation of shock losses for a choked branch of a loss curve with change of the exit static pressure

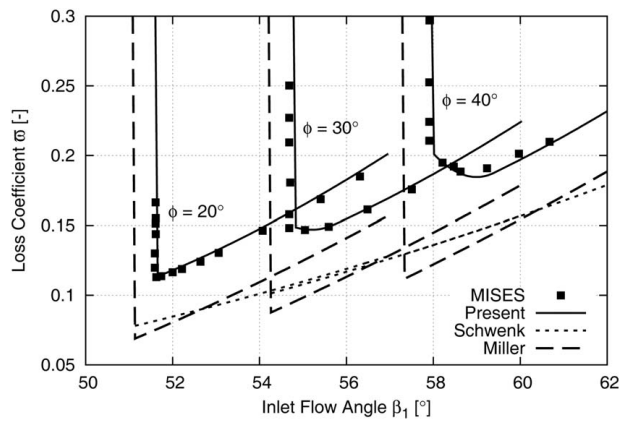


Fig. 19 Comparison of models

phenomenon did not produce the expected improvement. However, the discrepancy is significant only for low values of the exit pressure, which are not of practical importance.

Comparison With Previous Models

When it comes to the standard models, the comparison of shock loss results for a transonic compressor rotor [13] given in Ref. [10] shows surprisingly good agreement of the method of Schwenk et al. [2] and satisfactory agreement of the method of Miller et al. [1] with experimental results. Therefore, these models were selected for the comparison with the present work. Unlike the comparison in Ref. [10], here only two-dimensional cascade cases are considered to avoid the influence of other two- and three-dimensional flow effects. Since the aforementioned models consider only DCA airfoils, the cascade cases in Fig. 14 will be discussed. Such models define losses only for unchoked operation with supersonic inflow. The choke angle is obtained according to Ref. [25] as explained in Ref. [11], while the losses in the choked mode of operation remain undetermined. However, such an approach predicts the choke angle only while the losses in the choked mode of operation remain unknown.

As can be seen in Fig. 19, the model of Miller et al. gives lower values of losses compared with MISES and the present model. According to the analysis of the data, here discussed only briefly, the model predicts the Mach number in point *b* well, while slightly underpredicting it in point *d*. However, the procedure for predicting the local inclination of the shock, $\theta(y)$, yields lower value of the total pressure drop in spite of its detailed numerical integration across the pitch. In the model of Schwenk et al., the Mach number in point *b* is taken as $M_b = M_1$, while M_d is slightly overpredicted. Since the representative Mach number before the shock is taken as an arithmetic mean of these two values, the losses are underpredicted despite the passage shock being treated as normal. As for the choke angle, its slight underprediction according to Ref. [25] is caused by the disregarding of non-isentropic and two-dimensional effects in the inlet part of the cascade. Compared with the methods above, the present model accounts for choked and unchoked operation, both with subsonic-supercritical and supersonic inflow. Additionally, it considers various airfoil types.

Application and Future Research

The application of the model in a throughflow code is not demonstrated owing to restrictions on the length of the paper; however, the necessary steps for application are given as follows:

- It is crucial to correct the shock loss for the axial velocity density ratio (AVDR); otherwise the efficiency will be underpredicted for most transonic rotors. For now, only a simple

parabolic correction is applied which decreases the basic loss value to 85% when AVDR = 1.1, and increases it to 125% when AVDR = 0.9; more sophisticated corrections will be included in future research. In contrast, the correction of the throat according to AVDR-related variation of the stream sheet thickness results in underprediction of the choke mass flow, and therefore should not be applied.

- Although viscous effects should be included, the correction of the throat according to the local boundary layer displacement thickness resulted in underprediction of the choked mass flow for the tested compressor cases.
- Modeling of choked flows should formally include the bounding of the inflow angle β_1 to β_1^{ch} , by limiting the axial velocity as in the approach of Casey and Robinson [26]. However, the increase of losses in the choked region will already perform such limiting to a certain extent.
- The occurrence of choked operation next to the unchoked portion of the blade span results in a sudden jump of losses across the span. Hence, a spanwise distribution of the choked loss $\varpi - \varpi_U$ should be smoothed out to provide numerical stability.
- The shock losses should not be considered as the only source of Mach number-related losses. Therefore, the additional influence of the Mach number on basic profile losses in the subcritical range of operation must be included.

As mentioned, the future research will encompass the operation of precompression blades and turbine airfoils.

Conclusion

This paper provides a detailed description of a new universal model for shock losses in axial compressor airfoil cascades. The adjustable physical model combined with an adaptive definition of airfoil geometry can be applied for various blade types and operating regimes. The process is modeled with theoretical relations for isentropic flows and shock waves, and the related procedures are capable of handling different flow configurations. The cascade geometry is described with two levels of approximation that are used separately for the flow model and estimation of the throat opening. The choke angle equations were obtained from a set of numerical cases computed with the MISES solver. Validation was performed considering numerical results for transonic cases with typical and atypical cascade geometries. The comparison shows the ability of the present model to predict accurately the performance of various cases when operating with different inflow angles and Mach numbers. Since the results are reliable and the model is numerically stable, it is highly suitable for application in axial compressor throughflow codes.

Conflict of Interest

There are no conflicts of interest.

Data Availability Statement

The authors attest that all data for this study are included in the paper.

Nomenclature

- c = chord length ($c = 1$)
- g = staggered blade spacing
- l = bow shock detachment length
- o = opening, throat
- p = pressure
- s = blade spacing
- t = maximum blade thickness

x = chord-wise coordinate
 y = coordinate normal to chord
 M = Mach number
 r_{LE} = leading-edge radius
 X_0 = distance from bow shock vertex to asymptote center
 A, a = area, critical area ratio
 K_M, Q_M = Mach number-related interpolation coefficients

Greek Symbols

β = relative flow angle
 γ = blade stagger (setting) angle
 ϵ = inlet suction side turning angle
 θ = shock wave inclination relative to inflow
 κ = blade angle
 λ_s = conic Mach wave angle relative to inflow
 μ = Mach angle $\mu = \arcsin(1/M)$
 ν = Prandtl–Meyer angle
 $\overline{\omega}$ = total pressure loss coefficient
 Π = local or overall total pressure ratio p_2^o/p_1^o
 ρ = density
 ϕ = camber angle

Subscripts

C = camber
 CN = choked, normal second passage shock at \overline{ml}
 CO = choked, oblique second passage shock at \overline{lh}
 f = maximum camber position
 J = junction of two circular arc camber segments
 M = merged part of first and second passage shocks
 s = sonic point
 S = suction side
 t = maximum thickness position
 U = unchoked, converging the unique incidence
 1 = inflow, end of the leading-edge contour
 2 = outflow, start of the trailing edge contour

Superscripts and Operators

ch = choke value
 cr = critical
 n = new value
 o = total state
 $'l''$ = ahead of/behind the shock wave
 $:=$ = assignment of value

Appendix A

The radii of the camber segments

$$R_{C1} = \frac{E_2}{C_E}, \quad R_{C2} = \frac{E_1}{C_E}, \quad C_E = C_1 E_2 + C_2 E_1 \quad (A1)$$

are calculated using constants

$$C_1 = \sin \lambda_1 - \sin \lambda_J, \quad C_2 = \sin \lambda_J - \sin \lambda_2 \quad (A2)$$

$$E_1 = \cos \lambda_J - \cos \lambda_1, \quad E_2 = \cos \lambda_J - \cos \lambda_2 \quad (A3)$$

where $\lambda_1 = \kappa_1 - \gamma$, $\lambda_J = \kappa_J - \gamma$, and $\lambda_2 = \kappa_2 - \gamma$. The junction position of the two segments is $x_J = R_{C1} C_1$. For the first arc segment, the maximum offset and its position are, respectively,

$$y_f = R_{C1} [1 - \cos(\kappa_1 - \gamma)], \quad x_f = R_{C1} \sin(\kappa_1 - \gamma) \quad (A4)$$

When $x_f < x_J$, the values x_f and y_f correspond to the real maximum camber.

For the second arc segment, analogous formulas are used.

Appendix B

Bow shock detachment parameters according to Ref. [4] are

$$\frac{y_s}{y_{Ss}} = \left(1 - \sigma \frac{p_0}{p_s} \cos \lambda_s\right)^{-1} \quad (B1)$$

$$\frac{X_0}{y_{Ss}} = \beta \frac{y_s}{y_{Ss}} \sqrt{\beta^2 \tan^2 \theta_s - 1} \quad (B2)$$

$$\frac{l}{y_{Ss}} = \frac{y_s}{y_{Ss}} (C + \tan \lambda_s) - \tan \lambda_s \quad (B3)$$

These equations are computed using auxiliary expressions:

$$C = \beta \left(\beta \tan \theta_s - \sqrt{\beta^2 \tan^2 \theta_s - 1} \right) \quad (B4)$$

$$\beta = \sqrt{M^2 - 1} \quad (B5)$$

and functions fitted to graphical data from Ref. [4]:

$$\lambda_s = 11.675 + \frac{113.905}{M} - 341.288 e^{-M} \quad (B6)$$

$$\sigma = M^{0.7079} \exp[-1.0125 \cdot (M - 1)^{1.157}] \quad (B7)$$

$$\frac{p_0}{p_s} = [1 - \exp(-8.6418 \cdot M^{-2.645})]^{-1} \quad (B8)$$

$$\theta_s = 28.34 M^{-8.764} + 61.21 \quad (B9)$$

in the range $M \in (1, 2.5]$. The physical meaning of these variable is given in Ref. [4], and they are not explained here.

The asymptote angle of the hyperbolic bow shock is equal to the appropriate Mach angle $\mu = \arcsin(1/M)$, and the local inclination of the shock wave at position y is

$$\tan[\theta(y)] = \left(\beta^2 \frac{y}{y_{Ss}} \right)^{-1} \sqrt{\left(\frac{X_0}{y_{Ss}} \right)^2 + \left(\beta \frac{y}{y_{Ss}} \right)^2} \quad (B10)$$

Absolute values of X_0 , y_s , and l are determined with $y_{Ss} = r_{LE} \cos \lambda_s$, where r_{LE} is the leading-edge radius. Since the corresponding relative values from Eqs. (B1), (B2), and (B3) tend to infinity when M approaches unity, the input Mach number is limited to $M \geq 1.05$.

Appendix C

The flow deflection through an oblique shock is found as

$$\delta = \arctg \left\{ \left[\tan \theta \cdot \left(\frac{(\kappa + 1)M^2}{2(M^2 \sin^2 \theta - 1)} - 1 \right) \right]^{-1} \right\} \quad (C1)$$

with the singular case of $\delta = 0$ for $\theta = \pi/2$. The Mach number behind the shock wave, M_2 , then becomes

$$M_2 = \frac{1}{\sin(\theta - \delta)} \sqrt{\frac{(\kappa - 1)M^2 \sin^2 \theta + 2}{2\kappa M^2 \sin^2 \theta - (\kappa - 1)}} \quad (C2)$$

Relations for other flow variables can be found in Ref. [21].

Appendix D

The well-known Prandtl–Meyer function

$$\nu = \sqrt{\frac{\kappa+1}{\kappa-1}} \arctg \sqrt{\frac{\kappa-1}{\kappa+1}} (M^2 - 1) - \arctg \sqrt{M^2 - 1} \quad (D1)$$

is used together with its inverse solution given by Hall [22]:

$$M(\nu) = \sqrt{\frac{1 + 1.3604 q + 0.0962 q^2 - 0.5127 q^3}{1 - 0.6722 q - 0.3278 q^2}} \quad (D2)$$

where

$$q = \left(\frac{\nu}{\nu_{\max}} \right)^{2/3}, \quad \nu_{\max} = \frac{\pi}{2} \left(\frac{\kappa+1}{\kappa-1} - 1 \right) \quad (D3)$$

Appendix E

A theoretical expression that relates flow area to critical area ratio, $a = A/A_{cr}$, with the local Mach number M is

$$a(M) = \frac{A}{A_{cr}} = \frac{1}{M} \left[\frac{1 + (\kappa - 1)M^2/2}{1 + (\kappa - 1)/2} \right]^{(\kappa+1)/2(\kappa-1)} \quad (E1)$$

The approximate inverse solutions of this function are

$$M(a) = \frac{1}{\exp \sqrt{(a-1)/0.717}}, \quad M \leq 1 \quad (E2)$$

and

$$M(a) = 1 + 1.21146(a-1)^{0.5103}, \quad M > 1 \quad (E3)$$

For consistency, these approximate expressions are applied in both directions of calculation, $M(a)$ and $a(M)$, whereas the theoretical equation (E1) is not utilized.

Appendix F

The detachment parameters y_s , X_0 , and l in point b are again estimated by Eqs. (B1), (B2), and (B3), respectively, recalculated to absolute values according to r_{LE} and then corrected as

$$y_s := k \cdot y_s, \quad X_0 := k \cdot X_0, \quad l := k \cdot l \quad (F1)$$

The correction factor k will alter the basic single body related detachment values for the effects of repetitive cascade geometry

$$k = \left[1 + C_g \left(\frac{g}{l} \right) \cdot \sin(\beta_1 - \beta_1^{\text{ch}}) \right] \quad (F2)$$

where $C_g = 5$. This equation is based on a large number of cases calculated by MISES, including the examples demonstrated in the main part of the paper.

It should be noted that this correction is not used when the detachment parameters in point o are determined. Considering that the Mach number $M_o = M_1$ can be significantly lower than M_b owing to the suction side expansion, the additional correction would lead to overprediction of the related detachment parameters.

References

- [1] Miller, G. R., Lewis, G. W., and Hartmann, M. J., 1961, "Shock Losses in Transonic Compressor Blade Rows," *ASME J. Eng. Power*, **83**(3), pp. 235–241.
- [2] Schwenk, F. C., Lewis, G. W., and Hartmann, M. J., 1957, "A Preliminary Analysis of the Magnitude of Shock Losses in Transonic Compressors," NACA Report, RM E57A30.
- [3] Miller, G. R., and Hartmann, M. J., 1958, "Experimental Shock Configurations and Shock Losses in a Transonic-Compressor Rotor at Design Speed," NACA Report, RM E58A14b.
- [4] Moeckel, W. E., 1949, "Approximate Method for Predicting Form and Location of Detached Shock Waves Ahead of Plane or Axially Symmetric Bodies," NACA Report, TN 1921.
- [5] Klapproth, J. F., 1950, "Approximate Relative-Total-Pressure Losses of an Infinite Cascade of Supersonic Blades With Finite Leading-Edge Thickness," NACA Report, EM E9L21.
- [6] Bloch, G. S., Copenhaver, W. W., and O'Brien, W. F., 1999, "A Shock Loss Model for Supersonic Compressor Cascades," *ASME J. Turbomach.*, **121**(1), pp. 28–35.
- [7] Schoeiri, M. T., 1998, "Shock-Loss Model for Transonic and Supersonic Axial Compressors With Curved Blades," *J. Propul. Power*, **14**(4), pp. 470–478.
- [8] Boyer, K. M., and O'Brien, W. F., 2003, "An Improved Streamline Curvature Approach for Off-Design Analysis of Transonic Axial Compression Systems," *ASME J. Turbomach.*, **125**(3), pp. 475–481.
- [9] Koenig, W. M., Hennecke, D. K., and Fotner, L., 1994, "Improved Blade Profile Loss and Deviation Angle Models for Advanced Transonic Compressor Bladings: Part I—A Model for Subsonic Flow," ASME Paper No. 94-GT-335.
- [10] Aguirre, H. A., Pachidis, V., and Templelexis, I., 2019, "An Analytical Shock-Loss Model Fully Integrated to a Streamline Curvature Method for Axial-Flow Compressors," ASME Paper No. GT2019-91701.
- [11] Lichtfuss, H. J., and Starken, H., 1974, "Supersonic Cascade Flow," *Prog. Aerosp. Sci.*, **15**, pp. 37–149.
- [12] Moore, R. D., and Reid, L., 1980, "Performance of Single-Stage Axial-Flow Transonic Compressor With Rotor and Stator Aspect Ratios of 1.19 and 1.26 Respectively, and With Design Pressure Ratio of 2.05," NASA Report, NASA-TP-1659.
- [13] Urasek, D. C., Gorrell, W. T., and Cunnann, W. S., 1979, "Performance of Two-Stage Fan Having Low-Aspect-Ratio, First-Stage Rotor Blading," NASA Report, TP-1493.
- [14] Fellerhoff, J., 2010, "Entwicklung eines parametrischen Profilgenerators zur Beschreibung von 2-D Profilschnitten in Turbomaschinenbeschauungen," Semester thesis, Institute for Flight Propulsion, Technische Universität München.
- [15] Aungier, R. H., 2003, *Axial-Flow Compressors, A Strategy for Aerodynamic Design and Analysis*, ASME Press, New York.
- [16] Lieblein, S., 1965, "Experimental Flow in Two-Dimensional Cascades," *Aerodynamic Design of Axial-Flow Compressors*, I. A., Johnsen, and R. O., Bullock, eds., Vol. SP-36, NACA Report, pp. 183–225.
- [17] Taylor, W. E., Murrin, T. A., and Colombo, R. M., 1970, "Systematic Two-Dimensional Cascade Tests, 2. Multiple Circular Arc Hydrofoils," NASA Report, CR-72499.
- [18] Drela, M., and Youngren, H., 1998, *A User's Guide to MISES*, MIT Computational Aerospace Sciences Laboratory, Cambridge, MA.
- [19] Jansen, W., and Moffat, W. C., 1967, "The Off-Design Analysis of Axial-Flow Compressors," *ASME J. Eng. Power*, **89**(4), pp. 453–462.
- [20] Lieblein, S., 1959, "Loss and Stall Analysis of Compressor Cascades," *ASME J. Basic Eng.*, **81**(3), pp. 387–400.
- [21] Ames Research Staff, 1953, "Equations, Tables and Charts for Compressible Flow," NACA Report, NACA 1135.
- [22] Hall, I. M., 1975, "Inversion of the Prandtl–Meyer Relation," *Aeronaut. J.*, **79**(777), pp. 417–418.
- [23] Schnoes, M., 2020, "Eine Auslegungsmethodik fuer mehrstufige Axialverdichter auf Basis einer Profildatenbank," Ph.D. thesis, Fakultät fuer Maschinenbau, der Ruhr-Universität, Bochum.
- [24] Cumpsty, N. A., 1989, *Compressor Aerodynamics*, Longman, Harlow.
- [25] Levine, P., 1956, "Two Dimensional Inflow Conditions for a Supersonic Compressor With Curved Blades," Aeronautical Research Laboratory, WADC TR 55-387.
- [26] Casey, M., and Robinson, C., 2010, "A New Streamline Curvature Throughflow Method for Radial Turbomachinery," *ASME J. Turbomach.*, **132**(3), p. 031021.